Original Paper

A mathematical diffusion model of carbon isotopic reversals inside ultra-tight Longmaxi shale matrixes

Bao-Jian Shen [a, b, *], Zhi-Liang He [a, c], Cheng Tao [a, b], Jin-Cai Shen [d], Zong-Quan Hu [a, e], Zhi-Ming Li [a, b], Yuan-Hao Cao [f], Wei Chen [f, **]

[a] State Key Laboratory of Shale Oil and Gas Enrichment Mechanisms and Effective Development, SINOPEC, Beijing, 100083, China
[b] Wuxi Petroleum Geology Institute, SINOPEC Petroleum Exploration and Production Research Institute, Wuxi, Jiangsu 214126, China
[c] China Petroleum & Chemical Corporation, Beijing, 100728, China
[d] Chongqing Fuling Shale Gas Exploration and Development Co., Ltd., SINOPEC, Chongqing, 408014, China
[e] Petroleum Exploration and Production Research Institute, SINOPEC, Beijing, 100083, China
[f] School of Energy, Soochow University, Suzhou, Jiangsu 215006, China

A R T I C L E   I N F O

A B S T R A C T

Developing mathematical models for high Knudsen number (K_n) flow for isotopic gas fractionation in tight sedimentary rocks is still challenging. In this study, carbon isotopic reversals ($\delta^{13}C_1 > \delta^{13}C_2$) were found for four Longmaxi shale samples based on gas degassing experiments. Gas in shale with higher gas content exhibits larger reversal. Then, a mathematical model was developed to simulate the carbon isotopic reversals of methane and ethane. This model is based on these hypotheses: (i) diffusion flow is dominating during gas transport process; (ii) diffusion coefficients are nonlinear depending on concentration gradient. Our model not only shows a good agreement with isotopic reversals, but also well predicts gas production rates by selecting appropriate exponents m and m^* of gas pressure gradient, where m is for ^{12}C and m^* is for ^{13}C. Moreover, the ($m-m^*$) value has a positive correlation with fractionation level. ($m_1-m_1^*$) of methane are much higher than that of ethane. Finally, the predicted carbon isotopic reversal magnitude ($\delta^{13}C_1-\delta^{13}C_2$) exhibits a positive relationship with total gas content since gas in shale with higher gas content experiences a more extensive high K_n number diffusion flow. As a result, our model demonstrates an impressive agreement with the experimental carbon isotopic reversal data.
© 2022 The Authors. Publishing services by Elsevier B.V. on behalf of KeAi Communications Co. Ltd. This is an open access article under the CC BY-NC-ND license (http://creativecommons.org/licenses/by-nc-nd/4.0/).

1. Introduction

Stable carbon isotopic compositions of shale gas provide a unique way to quantitatively trace the gas generation and evolution processes, as well as gas migration patterns (Schoell, 1983; Tang et al., 2000; Xia and Tang, 2012; Xia et al., 2013; Cao et al., 2019; Li et al. 2020, 2021). Isotope geochemistry has been used as a tool for unconventional gas exploration. For example, the gas molecular (e.g., $C_1/(C_2+C_3)$) and stable isotopic (e.g., $\delta^{13}C_1$) composition of produced shale gases can be used to distinguish thermogenic and biogenic sources (Györe et al., 2018; Milkov and Etiope, 2018;

Zhang et al., 2020b). Carbon isotope-composition distribution patterns (e.g., isotopic reversals: $\delta^{13}C_1 > \delta^{13}C_2$) have been reported for Barnett, Fayetteville, and Triassic shale wells, which are the best productive shale reservoirs in North America (Rodriguez and Philp, 2010), as well as Longmaxi shale reservoirs in China (Milkov et al., 2020).

Full reversal ($\delta^{13}C_1 > \delta^{13}C_2 > \delta^{13}C_3$) and partial reversal ($\delta^{13}C_1 > \delta^{13}C_2 < \delta^{13}C_3$) of carbon isotopes have been found for the shale gas with different mixtures, such as organic and inorganic genetic gas, gas with the same origin but generated at different stages, and gas of different origins but the same type (Zhang et al., 2018). Different geochemical and physical processes, hydrocarbon generation and evolution, are experienced for Longmaxi shale gas and isotopic reversal of gases are considered to be of a thermogenic origin (Cao et al., 2018; Feng et al., 2020). Burruss and Laughrey postulated that the isotopic reversals were due to the mixing of gases combined with Rayleigh fractionation during redox reactions (Burruss and

Laughrey, 2010). Water-hydrocarbon reactions in high maturity shale may also account for isotopic reversals (Zumberge et al., 2012). In addition, carbon isotopes become reversed when the secondary gases from the retained liquid hydrocarbon cracking mix with the primary gases from the kerogen cracking (Zhang et al., 2014). However, the effect of the gas diffusion in porous media on isotopic gas reversals is still not well understood. The correlation between the gas content and flow transport in confined pore space and carbon isotopic reversals has not been well explored.

Gas compositions predominantly depend on its origin, but they can also be affected by sampling process, modality of gas occurrence, proportions of free and desorbed gases, and gas transport characteristics (e.g., diffusion and slip flow) etc. (Milkov et al., 2020). Even though extensive researches have been conducted to study the fractionation of carbon isotope in tight shale, there are still limited mathematical models that were developed to physically describe gas fractionation during gas degassing process, especially the reversal of carbon isotopes (Burruss and Laughrey, 2010; Li et al., 2021). Since micropore and mesopore are dominating in highly matured shale matrix and the permeability of shale could be lower to the level of nano-Darcies (Dai et al., 2014; Song et al., 2015; Deng et al., 2016; Wang et al., 2018), gas transported inside tight shale deviates from the laws of conventional continuum flow (Darabi et al., 2012; Liu et al., 2016a; Xia et al., 2017; Labed et al., 2018). Molecular diffusion (e.g., high K_n flow) are dominating inside nano-sized pore space as pressure drops (Liu et al. 2015, 2019; Rasoul and Mahmoud, 2017; Sun et al., 2019). Krooss et al. proposed that gas transport mechanism (e.g., diffusion) definitely accounts for the highest potential for molecular and isotopic fractionation effects (Krooss and Leythaeuser, 1997). During the diffusion process, $^{13}CH_4$ and $^{13}C_2H_6$ with higher physical mass have lower mobility than $^{12}CH_4$ and $^{12}C_2H_6$, respectively. Momentum and energy exchanged during molecule and pore wall collision could manifest diffusion velocity difference among molecules (Anderson, 1989; Anzini et al., 2019), which results in the accumulation of ^{13}C molecules trapped in a shale system and increases the carbon-isotope value (Pernaton et al., 1996; Xia and Tang, 2012). Moreover, competitive adsorptions exist in the pore surface for isotopic molecules due to their mass difference. Heavier $^{13}CH_4$ and $^{13}C_2H_6$ molecules are preferably adsorbed on pore surfaces compared to their lighter isotopic molecules (Zhang and Krooss, 2001; Liu et al., 2016b; Qin et al., 2017). As gas degassing process continues (i.e., shale internal pressure decreased), gas adsorption/desorption equilibrium shifts to desorption direction and different isotopic gases exhibit different desorption rates. $^{12}CH_4$ molecules with lower desorption activation energy have higher probability to release from pore wall, which leads to lighter molecule enrichment in the produced gases in the beginning of production (Zhang et al., 2020b).

Indeed, gas molecules with different molecular weights mitigate at different rates in nano-sized pores when they are subjected to temperature or pressure gradients. The advection−diffusion models are often employed, which is based on linear addition of gas diffusion by Fick's law and advection, for gas fractionation in low porous media permeability (Ding et al., 2017). For slip flow (0.01 < K_n < 0.1), the fractionation effect from advection gradually decreases (Sano and Fischer, 2013). For diffusion flow (K_n > 10), the mean free path of gas molecules is much higher than pore diameters and collisions between gas molecules and pores are well dominating inside the nanopore system (Wang et al., 2018). Diffusive fractionation of isotopic gases occurs when diffusion coefficient ratio $D/D*$ is not equal to 1, where D and $D*$ are the diffusion coefficients of isotopologues (e. g., $^{12}CH_4$ and $^{13}CH_4$) (Li et al., 2021). Since the molecular mean free path (λ) and average velocity (v) of gas molecules are the functions of temperature and

pressure (Gao et al., 2016), the diffusion coefficient is no longer a constant and nonlinear diffusion occurs inside the shale matrix as thermal or pressure gradient changes (Zhang et al., 2019). Since the driving force for the molecular diffusion is continuously changing as gas diffusion is going on (Ganti et al., 2017), it is still challenging to quantitatively estimate the diffusion coefficient of shale gas, especially when thermal or pressure gradient changes.

Recently, continuum flow models have been developed to describe the fractionation of isotopic methane gases in gas production process. Many factors such as porosity, gas pressure, gas adsorption/desorption behaviors were considered. El-Zehairy et al. (2019) and Lei et al. (2018) focused on the effect of microstructural parameters of nonlinear flow. Gao et al. (2017) developed a model considering gas adsorption/desorption to predict the gas production. However, limited studies took account the effect of parameters such as TOC and moisture content into gas flow models. It is still challenging to build a mathematic model to consider these parameters. The analysis of numerous variables also brings challenges to the simplification and utilization of the models. Besides, transition flow (0.1 < K_n < 10) models, which incorporated slip and diffusion flow, were used to predict the methane isotopic gas fractionation during thermal stimulated conditions (Deng et al., 2015; Zhang et al., 2019). Pure diffusion models were also used to describe isotopic gas fractionation inside the confined pores (Richter et al., 2005; Patzek et al., 2013). However, the diffusion coefficients in some models are assumed to be constant values (Richter et al., 2005; Xia and Tang, 2012). Actually, diffusion coefficients for high K_n number flow combine the effects from Knudsen diffusion, bulk diffusion, and surface diffusion, which exhibit a strong nonlinear property when shale internal pressure decreases (Richter et al., 2005; Xia and Tang, 2012; Wu et al., 2016). In addition, there are still insufficient mathematical models to explicitly incorporate both isotope and molecular fractionation simultaneously introduced by nonlinear diffusion, and the dynamic carbon isotopic reversal process has not been numerically analyzed.

In this study, a concentration/pressure-dependent continuous flow model was developed to describe the carbon isotopic reversal characteristics. First, canister experiments of four shale cores were conducted to measure the carbon isotopic reversals of methane and ethane gases. Then, a nonlinear mathematical model of carbon isotopic reversals of methane and ethane was developed and compared with experimental data. Moreover, gas production rates of methane and ethane isotopic gases of four samples were numerically simulated. In addition, the correlation between the exponent difference ($m−m*$) and magnitude of carbon isotopic reversals ($\delta^{13}C_1−\delta^{13}C_2$) and gas diffusion condition was investigated and analyzed.

2. Shale gas canister experiments

In this study, canister experiments were conducted to measure the gas compositions of the four shale cores (Weiye1, Weiye2, Weiye3, and Jinye) with height of 0.20 m and diameter of 0.10 m, collected from Fuling, Chongqing, China. As shown in Fig. 1, the test procedure was similar to the experiments conducted by Chen et al. (2019). The canister was first preheated at a constant temperature of 55 °C. The sealed canister was connected to a volume displacement apparatus (glass collection cylinder) to collect the degassing gas (Fig. 1). The glass collection cylinder (125 mL) was substituted by a new one after saturated brine (about 100 mL) in the cylinder was replaced by gas. This procedure was continued until the end of the experiment. With the sharp decline of gas production rate (after 4 h of heating at 55 °C), the samples were heated to 110 °C in order to extract the remaining absorbed gases. The experiments last until instantaneous gas volume became very small (data fluctuated
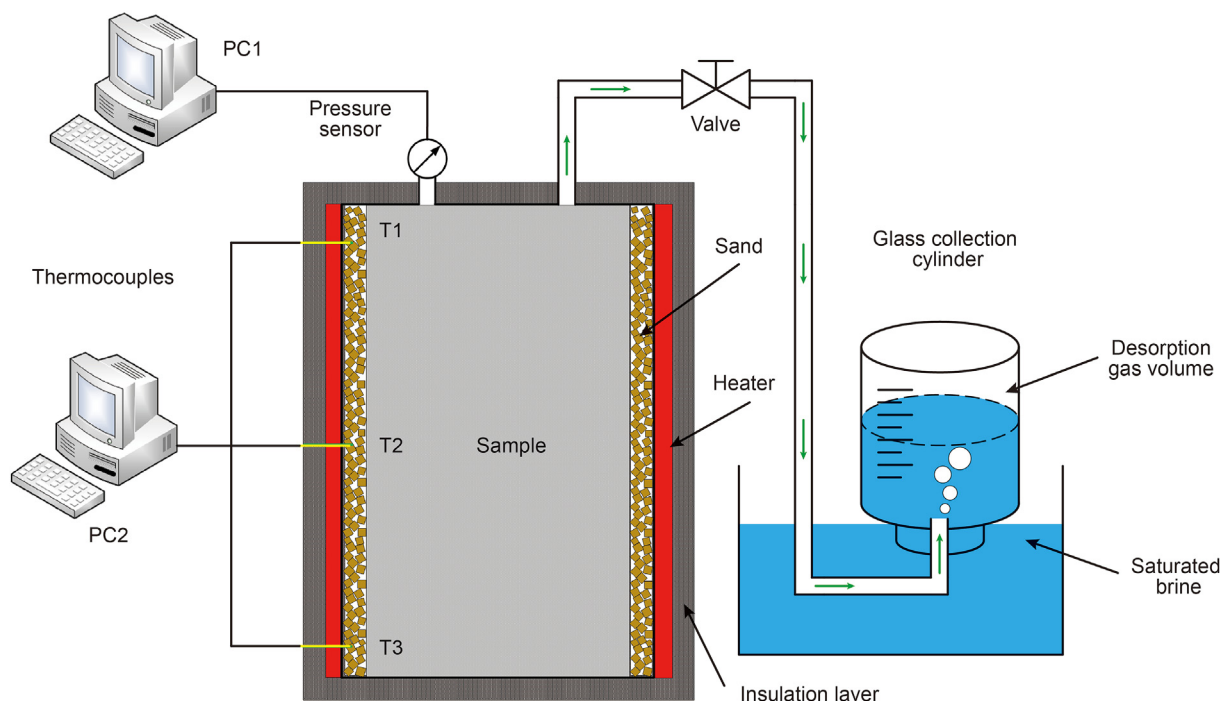
Fig. 1. Schematic model of the canister desorption apparatus. Adopted and modified from Chen et al. (2019).

within ±0.1% range in the last half hour). More details of the experiments can be found in studies of Chen et al. (2019).

After experiments, the total gas production of the four shale samples were estimated and the collected gas samples were sent to State Key Laboratory of Shale Oil and Gas Enrichment Mechanisms and Effective Development (Sinopec), Wuxi, China for bulk gas analysis. The gas compositions (including CH_4, C_2H_6, N_2, H_2, and CO_2) were measured using VARIAN 3800 gas chromatograph (GC). The carbon isotopic measurements were performed with an Agilent 7890 gas chromatography coupled to a Thermo Finnigan MAT 253 isotope ratio mass spectrometer (IRMS) system. The gases including CH_4 and C_2H_6 were separated with an HP Plot Q column (30 m × 0.32 mm × 20 μm). The GC was programmed to start at 40 °C for 2 min, followed by a heating rate of 5 °C/min to 80 °C, then a gradient of 10 °C/min to 100 °C holding constant for 2 min. Finally, the GC was heated to 240 °C with a gradient of 20 °C/min and kept at 240 °C for 3 min. The split ratio was 15:1. The measure procedures were performed according to Chinese national reference material (GBW04480). The relative standard deviation of the measurement is 0.2‰.

3. Model of the nonlinear isotopic gas flow in tight shale rocks

After being retrieved from underground, the shale cores were exposed to ambient pressure. Shale has extremely low permeability on the order of nano-darcy (Gao et al., 2019). The average pore diameters of the shale samples were obtained using BJH method, based on the low temperature nitrogen adsorption/desorption isotherms. The average pore diameters of Weiye1, Weiye2, Weiye3 and Jinye shale samples are 7.90 nm, 7.67 nm, 8.34 nm, and 5.23 nm, respectively. Thus, as process pressure drops to close to ambient pressure, the mean free path of gas is greater than the shale pore diameter, and gas transport inside the shale shifts to high K_n diffusion flow. Chen et al. found that diffusion flow was dominating inside the shale during canister experiments (Chen

et al., 2019). As a result, it is reasonable to assume that adsorption/desorption and diffusion are the main flow characteristics during the degassing process (Fig. 2, adopted and modified from Cao et al. (2019)).

Thus, a one-dimensional nonlinear mass diffusion equation of carbon isotopes of methane and ethane with different molecular diffusivities in a cylindrical shale core can be written as

$$
\begin{cases}
\dfrac{\partial C_1}{\partial t} = \dfrac{1}{r}\dfrac{\partial}{\partial r}\left(rD_1\dfrac{\partial C_1}{\partial r}\right) \\[2mm]
\dfrac{\partial C_1^*}{\partial t} = \dfrac{1}{r}\dfrac{\partial}{\partial r}\left(rD_1^*\dfrac{\partial C_1^*}{\partial r}\right)
\end{cases}
\text{ and }
\begin{cases}
\dfrac{\partial C_2}{\partial t} = \dfrac{1}{r}\dfrac{\partial}{\partial r}\left(rD_2\dfrac{\partial C_2}{\partial r}\right) \\[2mm]
\dfrac{\partial C_2^*}{\partial t} = \dfrac{1}{r}\dfrac{\partial}{\partial r}\left(rD_2^*\dfrac{\partial C_2^*}{\partial r}\right)
\end{cases}
\tag{1}
$$

where subscript 1 denotes methane gas and subscript 2 denotes ethane gas, r is radius of the shale core (m), D is effective diffusion coefficient (m²/s), t is time (s), ρ is gas density (kg/m³), and C is gas concentration inside the shale cores (kg/m³). Considering gas adsorption/desorption inside the nano-pore surface, C is expressed as (Cui et al., 2009):

$$
C = \rho\varphi + (1-\varphi)q
\tag{2}
$$

where φ is porosity and q is adsorbed gas density per unit sample volume (kg/m³). In this model, the gas flow in tight porous shale is assumed to be dominated by gas diffusion. Therefore, substituting Eq. (2) into the general form of Eq. (1), a simplified equation containing ρ can be obtained (Cui et al., 2009):

$$
\frac{\partial}{\partial t}(\rho\varphi + (1-\varphi)q) = \varphi\frac{1}{r}\frac{\partial}{\partial r}\left(rD\frac{\partial\rho}{\partial r}\right)
\tag{3}
$$

The effective diffusion coefficient, which is not a constant during the gas degassing process, is a density-gradient-dependent parameter. It can be expressed as
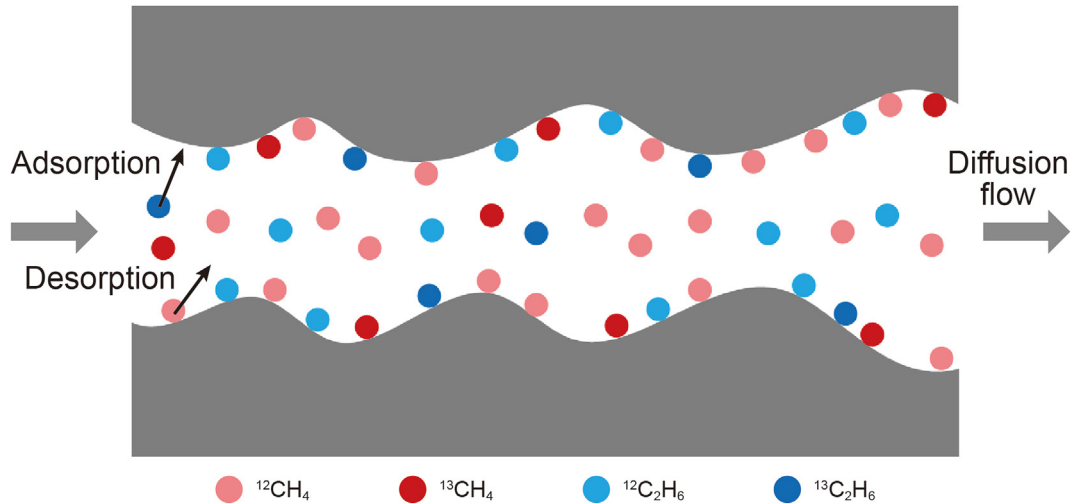
Fig. 2. Gas flow in the shale pore system during degassing process, adopted and modified from Cao et al. (2019).

$$D = B\left(\frac{\partial \rho}{\partial r}\right)^n \tag{4}$$

Since $\rho = \frac{MP}{zRT}$, Eq. (4) could be written as a function of pressure gradient. Thus, it can be written as $B\left(\frac{\partial \rho}{\partial r}\right)^n = A\left(\frac{\partial p}{\partial r}\right)^m$, where p is the gas pressure (Pa) at radius r of the shale sample; A, B, n, and m are assumed to be constants.

Substituting Eq. (4) into Eq. (3) yields

$$\frac{\partial}{\partial t}(\rho \varphi + (1-\varphi)q) = \varphi \frac{1}{r}\frac{\partial}{\partial r}\left(rA\frac{M}{zRT}\left(\frac{\partial p}{\partial r}\right)^{m+1}\right) \tag{5}$$

According to Cui et al. (2009), gas adsorption isotherms in shale matrix can be approximated by the Langmuir isotherm as

$$q = \frac{\rho_r}{V_{std}}\frac{pV_L}{p+p_L} \tag{6}$$

where ρ_r is the density of shale (kg/m³), V_{std} is the gas volume (m³/kg) at standard pressure (1 bar) and standard temperature (273.15 K), p_L and V_L are the Langmuir pressure (Pa) and volume (m³/kg), respectively.

Substituting Eq. (6) into Eq. (5) yields

$$\frac{M}{zRT}\frac{\partial p}{\partial t} + \frac{(1-\varphi)}{\varphi}\frac{\rho_r}{V_{std}}\frac{p_L V_L}{(p+p_L)^2}\frac{\partial p}{\partial t} = \frac{1}{r}\frac{\partial}{\partial r}\left(r\frac{AM}{zRT}\left(\frac{\partial p}{\partial r}\right)^{m+1}\right) \tag{7}$$

Eq. (7) can be simplified as

$$c_1\frac{\partial p}{\partial t} = \frac{1}{r}\frac{\partial}{\partial r}\left(rc_2\left(\frac{\partial p}{\partial r}\right)^{m+1}\right) \tag{8}$$

where $c_1 = \frac{M}{zRT} + \frac{(1-\varphi)}{\varphi}\frac{\rho_r}{V_{std}}\frac{p_L V_L}{(p+p_L)^2}$ and. $c_2 = \frac{AM}{zRT}$

The boundary conditions of Eq. (8) regarding the shale core during gas degassing process are given as

$$p(r=r_0,\ t) = p_0,\ \frac{\partial p}{\partial r}_{(r=0,\ t)} = 0 \tag{9}$$

where p_0 is ambient pressure (Pa), and r_0 is the radius of the shale core (m). In order to simplify Eq. (8), dimensionless variables

(dimensionless distance and time) can be defined by using self-similarity method (Monteiro et al., 2012):

$$\xi = \frac{r-r_0}{(\chi p^m(t-t_0))^{\frac{1}{m+2}}} \text{ and } \tau = \frac{\left(\frac{r^{m+2}}{\chi p^m}\right)}{t-t_0} \tag{10}$$

where $\chi = \frac{c_2}{c_1}$, t_0 is the initial experimental time.

Substituting Eq. (10) into Eq. (8), an ordinary differential equation can be obtained:

$$\frac{\xi p^m}{m+2}\frac{\partial p}{\partial \xi} + \frac{1}{\xi}\left(\frac{\partial p}{\partial \xi}\right)^{m+1} + (m+1)\left(\frac{\partial p}{\partial \xi}\right)^m\frac{\partial^2 p}{\partial \xi^2} = 0 \tag{11}$$

Let $f = \frac{p}{p_0} \Rightarrow p = fp_0$ and substitute it into the above equation. An ordinary differential equation of $f(\xi)$ can be given as follows:

$$\frac{\xi f^m}{m+2}\frac{\partial f}{\partial \xi} + \frac{1}{\xi}\left(\frac{\partial f}{\partial \xi}\right)^{m+1} + (m+1)\left(\frac{\partial f}{\partial \xi}\right)^m\frac{\partial^2 f}{\partial \xi^2} = 0 \tag{12}$$

Thus, the production rate from the shale core (Q, m³/s) can be estimated:

$$Q = Sj_n = S\left(rD\frac{\partial \rho}{\partial r}\right) \tag{13}$$

where S is the surface area of shale core (m²), j_n is the gas flux (m/s) through shale surface.

$$Q = Sj_n = S\left(r\frac{AM}{zRT}\left(\frac{\partial p}{\partial r}\right)^{m+1}\right)$$
$$= Sr\frac{AM}{zRT}\left(\frac{\partial p}{\partial \xi}\right)^{m+1}\chi^{-\frac{m+1}{m+2}}p^{-\frac{m(m+1)}{(m+2)}}(t-t_0)^{-\frac{m+1}{m+2}} \tag{14}$$

On the surface of the shale core sample, $r = r_0$, $p = p_0$,

let. $a = Sr\frac{AM}{zRT}\left(\frac{\partial p}{\partial \xi}\right)^{m+1}_{r=r_0}\chi^{-\frac{m+1}{m+2}}p^{-\frac{m(m+1)}{(m+2)}}$

Eq. (14) can be simplified as

$$Q = a(t-t_0)^{-\frac{m+1}{m+2}} \tag{15}$$

The production rates of carbon isotope of methane and ethane are shown respectively as:

$$\begin{cases} Q_1 = a_1(t-t_0)^{-\frac{m_1+1}{m_1+2}} \\ Q_1^* = a_1^*(t-t_0)^{-\frac{m_1^*+1}{m_1^*+2}} \end{cases} \text{ and } \begin{cases} Q_2 = a_2(t-t_0)^{-\frac{m_2+1}{m_2+2}} \\ Q_2^* = a_2^*(t-t_0)^{-\frac{m_2^*+1}{m_2^*+2}} \end{cases} \quad (16)$$

Isotope ratios are reported as δ-values defined as:

$$\begin{cases} \delta^{13}C_1 = \left(\dfrac{R_{1-sample}}{R_{standard}} - 1\right) \times 1000 \ (‰) \\ \delta^{13}C_2 = \left(\dfrac{R_{2-sample}}{R_{standard}} - 1\right) \times 1000 \ (‰) \end{cases} \quad (17)$$

Here R denotes the molecular ratio of $^{13}C/^{12}C$. Carbon isotope values are given with reference to the PDB (Pee Dee Belemnite) standard ($R_{standard}$).

$$R_{sample} = \frac{C^*}{C} = \frac{C^* \cdot G}{C \cdot G} = \frac{Q^*}{Q} \quad (18)$$

where C is gas concentration and G is total gas production rate.

Combining Eq. (17) and Eq. (16) together, isotope ratios can be obtained:

$$\begin{cases} \delta^{13}C_1 = b_1(t-t_0)^{\frac{m_1-m_1^*}{(m_1+2)(m_1^*+2)}} + d_1 \ (‰) \\ \delta^{13}C_2 = b_2(t-t_0)^{\frac{m_2-m_2^*}{(m_2+2)(m_2^*+2)}} + d_2 \ (‰) \end{cases} \quad (19)$$

where. $\begin{cases} b_1 = \dfrac{1000}{0.0112372} \dfrac{a_1^*}{a_1} \\ d_1 = -1000 \end{cases}$ and $\begin{cases} b_2 = \dfrac{1000}{0.0112372} \dfrac{a_2^*}{a_2} \\ d_2 = -1000 \end{cases}$

The total gas production (TGP, m^3) can be obtained by summing gas production at each measure step:

$$TGP = \begin{cases} \sum Q\Delta t/C = \sum a_1(t-t_0)^{-\frac{m_1+1}{m_1+2}}\Delta t \Big/ C_1 \\ \sum Q^*\Delta t/C^* = \sum a_1^*(t-t_0)^{-\frac{m_1^*+1}{m_1^*+2}}\Delta t \Big/ C_1^* \\ \sum Q\Delta t/C = \sum a_2(t-t_0)^{-\frac{m_2+1}{m_2+2}}\Delta t \Big/ C_2 \\ \sum Q^*\Delta t/C^* = \sum a_2^*(t-t_0)^{-\frac{m_2^*+1}{m_2^*+2}}\Delta t \Big/ C_2^* \end{cases} \quad (20)$$

where Δt is the time interval between two gas measurement steps (s).

This nonlinear gas flow model is developed by using self-similarity method, which could decrease the number of independent variables in the mathematical model and can significantly simplify the equations. Based on Eqs. (16) and (20), the values of m and m^*, which are the exponents of gas pressure gradient $\frac{\partial p}{\partial r}$ and $\frac{\partial p^*}{\partial r}$, respectively, can be quickly determined by fitting with experimental gas production data of methane and ethane. The m and m^* are the key parameters reflecting the nonlinear diffusion capacity of gases, which combine the effect of geophysical and geochemical parameters. Then, the scaling carbon isotope values of methane and ethane can be obtained based on Eq. (19), in which $m-m^*$ can well reflect isotopic gas fractionation.

4. Results and discussions

4.1. Gas composition of the produced gas

The gas concentration variation with diffusion time is a result of diffusive transport through the porous rocks. Due to the mass difference of gas molecules, the gas composition of expelled gas changes with time and there is an instantaneous differential value (molecular fractionations) for the degassing gas, as well as trace concentrations of noble gases. It is found that the produced gases primarily consist of CH_4, C_2H_6, H_2, and non-hydrocarbon gases (N_2 and CO_2). CH_4 is dominating among these gases, and it takes up more than 90% volume (Fig. 3). As discussed before, the gases mitigated inside pores in the form of molecular diffusion, and diffusivity differences among light and heavy molecules in multi-component gas mixtures resulted in fractionation of gas species (Cunningham and Williams, 1980). At the early stage of gas degassing, N_2 percentage is relatively high due to the dilution of air in the canister. After 50 min of heating, "lighter" gases such as CH_4 are rich in the produced gas induced by molecular diffusion in the pore systems. Lighter molecules diffuse faster and are easily desorbed from pore surfaces (Tang and Xia, 2011; Wu et al., 2015). As the experiment continues (after 240 min), the content of CH_4 gradually decreases, while the percentage of heavier gases (e.g., CO_2, C_{2+}) increases. This is more obvious for samples from Weiye shales. It is because that heavier gases are able to overcome the strong van der Waals forces and desorb from the pore surfaces as pressure decreases (Etminan et al., 2014). Thus, produced gas is correspondingly "lighter" at the early heating stage, and then enriched with "heavy" CO_2 and C_2H_6 molecules.

4.2. Gas content of shale samples

The accumulated degassing gas were also found for the four samples (Fig. 4). Weiye3 sample has the highest gas content (about 5.35 m^3/t), while Jinye shale has lowest gas content (about 1.76 m^3/t). This is due to the fact that Weiye3 sample has highest organic matters (e.g., kerogen) according to Table 1 in Appendix. The high maturity shale samples ($R_o > 2.5\%$) have well-developed pore system and have more well-developed small organic-hosted pores which provide numerous adsorption sites for gas molecules (Etminan et al., 2014; Yang et al., 2015). Weiye3 with high organic matter has abundant storage space for gas molecules and the gas content is correspondingly high (Zhang et al., 2020a). In addition, different fractionation characteristics of isotopic carbon gases are manifested by high K_n diffusion, which is closely linked to gas content (Shi et al., 2019).

4.3. Isotopic gas fractionation of methane and ethane

Recently carbon isotopic reversal has served as a promising indicator of the sweet-spot of shale gas (Ding et al., 2017). Even though the mechanism of the reversed gases is still controversial, the reversal is manifested during diffusion process. Based on the experiment, the methane and ethane isotopic composition during production was obtained and the fractionations of these two gases were calculated using Eq. (17).

It was found that carbon isotopic reversals ($\delta^{13}C_1 > \delta^{13}C_2$) occurred for four shale samples (Fig. 4). In addition, $\delta^{13}C_2$ fluctuates around −40‰, while $\delta^{13}C_1$ varies significantly among shale samples, especially for Weiye3 shales (from −36‰ to −10‰). It was also reported that for Longmaxi shale $\delta^{13}C_1$ value varied from −35‰ to −5‰, while the change of $\delta^{13}C_2$ value was insignificant compared to $\delta^{13}C_1$ (from −39‰ to −36‰) (Qin et al., 2017; Ma et al., 2020).
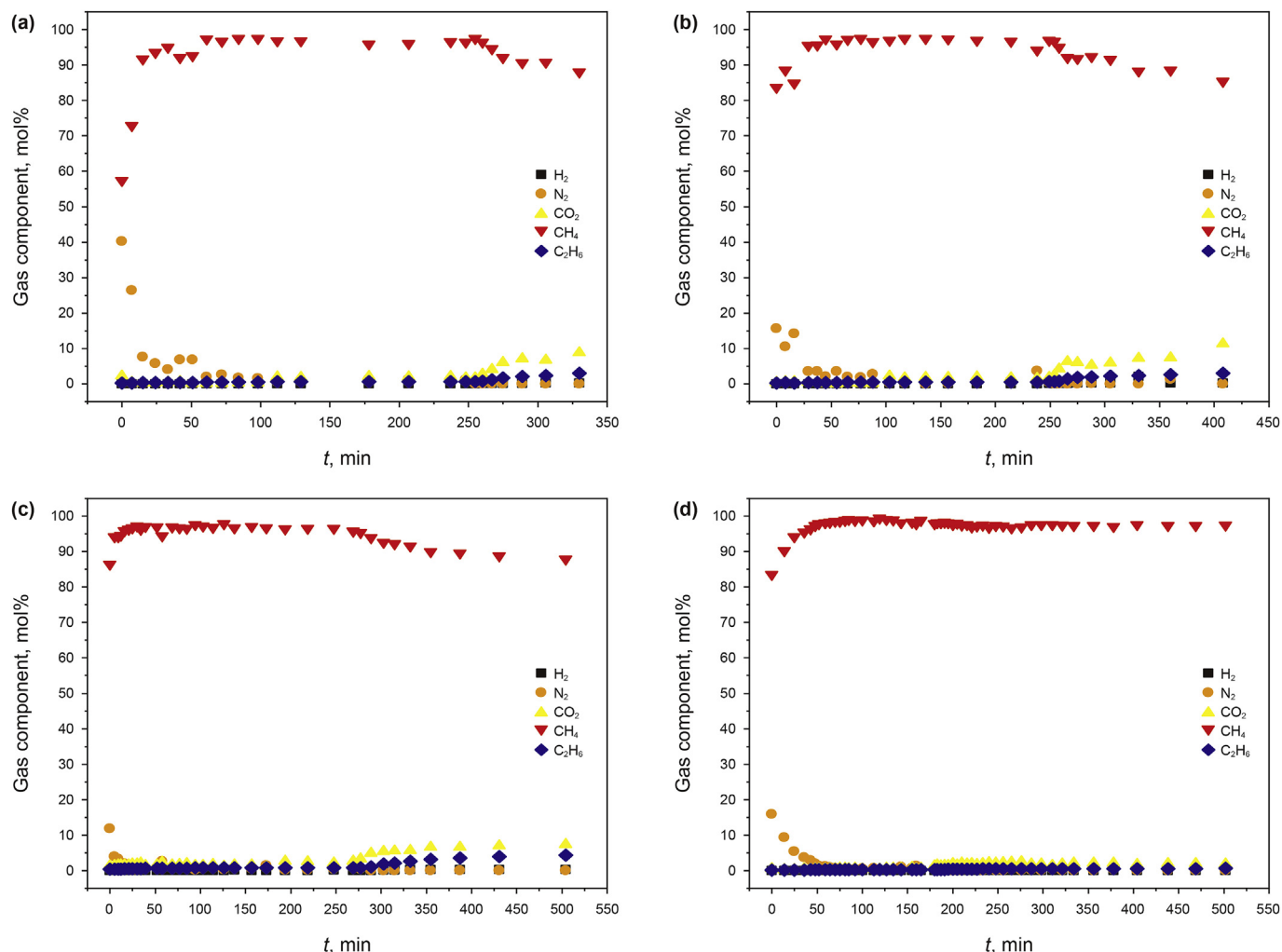
Fig. 3. Gas components over degassing time for (a) Weiye1, (b) Weiye2, (c) Weiye3 and (d) Jinye.

The mass difference between $^{13}C_2H_6$ and $^{12}C_2H_6$ molecules is insignificant compared to methane isotopes and their flow characteristics are less sensitive to pressure change (Strąpoć et al., 2006; Tang and Xia, 2011). Therefore, the fractionation fluctuation introduced by gas adsorption/desorption in the mineral surfaces or sedimentary organic matter (kerogen) and molecule−wall interaction diffusion is relatively low for ethane isotopes (Meng et al., 2016; Qin et al., 2017). Besides, biogenic and thermogenic gases are characterized by high methane percentage and low heavy hydrocarbon content, and the content of storage ethane is relatively low and fractionation changes driven by the concentration gradient are correspondingly insignificant (Ma et al., 2020). Therefore, the variations of $\delta^{13}C_2$ of the four shale samples are minor. Different from ethane isotopic gases, there is a more significant diffusion or adsorption/desorption action difference for methane isotopic gases. In the beginning, lighter $^{12}CH_4$ diffuses faster and are more easily desorbed from pore walls which causes fractionation (Zhang et al., 2018; Ma et al., 2020). At later degassing stage, desorption probability of $^{13}CH_4$ increases and they are triggered to leave pore surfaces to enrich in the produced gases as pressure drops. The ratio of $^{13}CH_4/^{12}CH_4$ increases and gases are richer with $^{13}CH_4$ at the late stage of production. The level of methane fractionation decreases as diffusion is going on. This is manifested in high gas content shale samples since fractionation caused by diffusion and adsorption/

desorption is more intensive. Krooss et al. also found that the degree of methane isotopic gas fractionation, due to molecular diffusion, increased as the TOC content increased in the shales (Zhang and Krooss, 2001).

Thus, the magnitude of carbon isotopic reversal ($\delta^{13}C_1−\delta^{13}C_2$) is nonlinearly increased as experiment is going on. Three Weiye shale reversals are in the range of 14.5 ‰−16.5‰, while the Jinye shale reversal is only around 4.9‰ after 300 min of heating. Shale samples with high organic matter have more isotopic methane gases stored inside the pore system, so the internal gas pressure is correspondingly higher after retrieved from formation reservoir. Actually, the methane flow in the shale with more gas content experiences significant K_n number change ΔK_n ($=K_{n\,\mathrm{intial}} − K_{n\,\mathrm{final}}$). In the beginning of the canister experiment, the mean free path of methane gas is relatively small (i.e., K_n number is relatively low) for shale with more gas content. As experiments approach to the end, the pressure gradient is very small as most of the gas is already depleted from the shale core, the mean free path of the gas becomes extremely large, and K_n is correspondingly high. As a result, gas in shale with higher gas content experiences a more extensive K_n diffusion flow (large ΔK_n) and the magnitude of reversal is correspondingly increased. The magnitude of reversal has a positive correlation with gas ΔK_n.
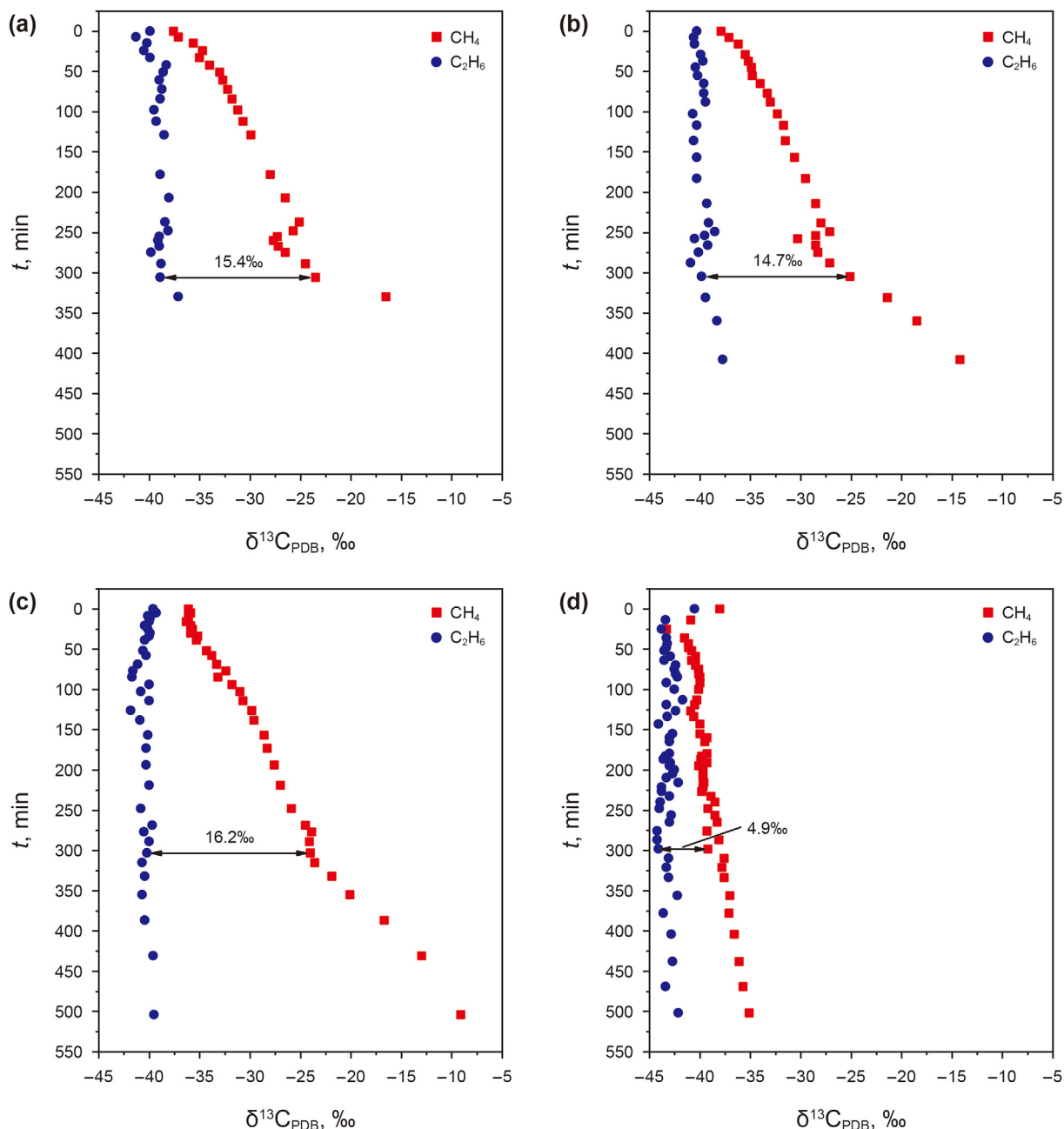
Fig. 4. $\delta^{13}C_{PDB}$ of CH$_4$ and C$_2$H$_6$ over time for (a) Weiye1, (b) Weiye2, (c) Weiye3 and (d) Jinye.

4.4. Simulation results

4.4.1. Scaling carbon isotopic reversal

Methane and ethane isotopic gases have different adsorption and mobility capacity, which cause carbon isotopic fractionation to occur during gas degassing process. The scaling fractionation of methane and ethane gases could be obtained by selecting approximate exponents m and m^* to match the experimental data, using MATLAB as the numerical solver. Firstly, the m_1 and a_1, m_1^* and a_1^*, m_2 and a_2, m_2^* and a_2^* were determined by fitting the experimental and scaling production rates of $^{12}CH_4$, $^{13}CH_4$, $^{12}C_2H_6$ and $^{13}C_2H_6$ according to Eq. (16). Then, the scaling $\delta^{13}C_1$ and $\delta^{13}C_2$ were calculated based on Eq. (19) and matched with the experimental results. As shown in Fig. 5, the scaling carbon isotopic reversals for methane and ethane generally matches the experimental data well, especially for the first 300 min. m_1 and m_1^* range from −1 to 0.3, while m_2 and m_2^* range from −1 to 0 depending on the shale samples. In addition, the differences between m and m^* are relatively small for both methane and ethane, demonstrating the fractionation of isotopic gases is a slow physical process. In other word, the diffusion capacity difference among the isotopic gases is very small in the confined pore space. In fact, m and m^* are the key parameters affecting the nonlinear gas fractionation. Geophysical and flow transport parameters, such as the tortuosity of the pore channels, thermal gradient, and high K_n flow effect etc., are the factors that affect m and m^* values (Monteiro et al., 2012).
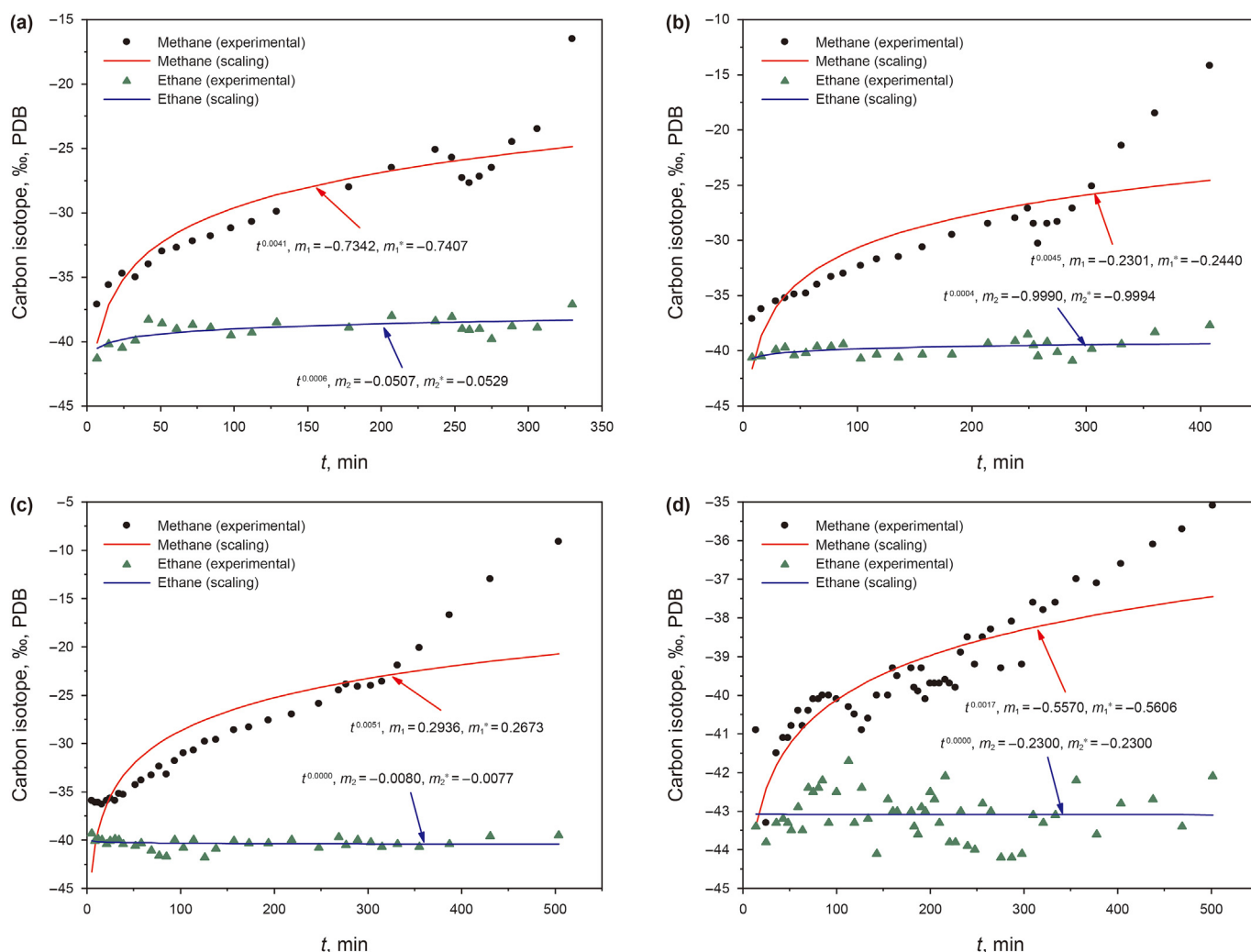
Fig. 5. Experimental and scaling methane and ethane carbon isotope compositions. (a) Weiye1, (b) Weiye2, (c) Weiye3, (d) Jinye.

For example, carbon isotopic reversal becomes larger as the degassing process is going. It is because gas transport gradually shifts to higher K_n diffusion flow and collisions between the molecules and pore walls become more significant as gas density inside the shale matrix decreases (internal pressure drop). Thus, the level of isotopic gas fractionation is gradually enhanced. Due to the different high K_n number diffusion flow inside the four shale samples, m_1, m_1^*, m_2, and m_2^* are different from each other, demonstrating different nonlinear diffusion processes exist as K_n number changes. Thus, exponents m and m^* generally reflect the nature and evolution of isotope flow fractionation characteristic in response to different shale samples.

4.4.2. Correlation of m−m* with carbon isotopic gas reversal

As discussed before, methane and ethane exhibit different fractionation characteristics when they are diffused inside the small pores of shale matrix. The difference between exponents m and m^*, which reflects the nonlinear diffusion capacity of gases, could serve as an indicator of the level of the carbon isotopic reversals. The $(m_1−m_1^*)$ values of four samples vary and are mainly located in the range of 0.005−0.03. In addition, $(m_1−m_1^*)$ are much higher than $(m_2−m_2^*)$ for the four shale samples (Fig. 6), especially for Weiye3. This means methane isotopic gases exhibit stronger
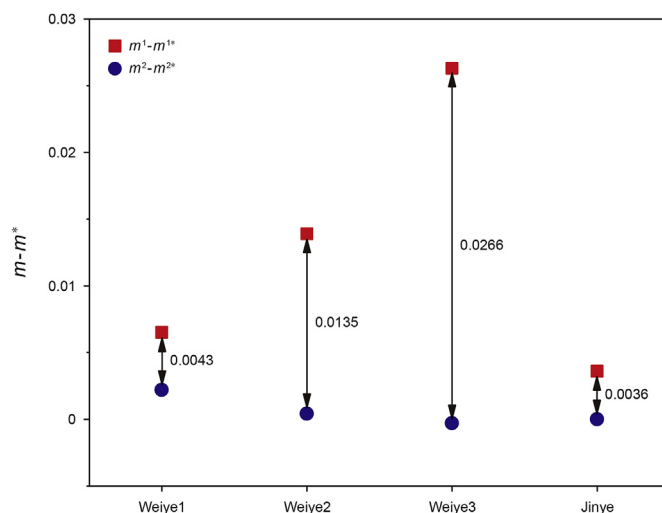

Fig. 6. Values of $(m−m^*)$ for methane and ethane gases.

nonlinear diffusion property than that of ethane. According to gas kinetic theory, diffusion coefficient variation in Knudsen regime is

affected by relative gas molecular weight difference (Di Felice, 2016). Isotopic gases with larger physical mass difference have different Knudsen-diffusivity. During diffusion process, the energy and moment loss difference is more significant for methane isotopic gas as the molecules collide or hop on pore walls. Thus, obvious fractionation variations are found for methane isotopes. Moreover, $(m_2-m_2^*)$ of the four shale samples are very small (almost close to 0), which means the fractionation status of ethane is almost constant and diffusion capacity of ethane isotopic gases (e.g., diffusion coefficient ratio, D_2/D_2^*) does not vary much. Among all the samples, Weiye 3 has the smallest $(m_2-m_2^*)$ values and the biggest carbon reversal with highest Δm_1 $(m_1-m_1^*)$. It is interesting that Weiye 3 with biggest $\Delta m_1-\Delta m_2$ has the highest carbon reversal characteristic $(\delta^{13}C_1-\delta^{13}C_2)$. As discussed before, shale with high gas content experiences diffusion flow with large ΔK_n changes, which is reflected by the $\Delta m_1-\Delta m_2$ values.

4.4.3. Scaling isotopic gas flow

Diffusive gas migration inside shales exhibits different production decline trends. According to Eq. (16), the scaling isotopic gas production rates of methane and ethane could be predicted, and the results are given in Fig. 7 and Fig. 8, respectively. The production rates of methane ($^{12}CH_4$) decline exponentially as $t^{-0.210}$, $t^{-0.435}$, $t^{-0.564}$, and $t^{-0.307}$, with the corresponding m_1 values of -0.7342, -0.2301, 0.2936, and -0.5570 for the four samples.

Similar decline trend was found for $^{13}CH_4$. The gas production rates decline quickly and then become very low as experiment goes on.

The experimental and scaling cumulative gas production of $^{12}CH_4$, $^{13}CH_4$, $^{12}C_2H_6$, and $^{13}C_2H_6$ were also compared, as shown in Fig. 9. The scaling results were matched well with the experimental results, which were calculated based on Eq. (20) after the determination of m_1, m_1^*, m_2 and m_2^*. Corresponding with variation of production rates, the increase in cumulative gas production gradually slowed down as time going on, and the cumulative gas production during gas degassing process also has the following order: Weiye3 > Weiye1 > Weiye2 > Jinye.

As discussed before, high K_n effect becomes more significant as pressure decreases. At this stage, gas concentration is small and gas flow is correspondingly low. In Fig. 7, it could be observed that Weiye3 has the highest initial gas production rate, 0.38 m³/day and 0.041 m³/day for $^{12}CH_4$ and $^{13}CH_4$, respectively, while it is only about 0.042 m³/day and 0.00047 m³/day for Jinye shale. Since there is more gas stored inside the Weiye3 shale matrix, the gas releasing rates are correspondingly higher. In addition, Weiye3 exhibits higher $^{13}CH_4/^{12}CH_4$ ratio changes during gas degassing experiments (0.01070 in the beginning and 0.0110 at the end), while it only ranges from 0.01075 to 0.01082 for Jinye shale. This coincides with K_n number changes of the samples. Shale with more methane content experiences a wider range of high K_n number diffusion flow and fractionation become larger as flow K_n number increases.
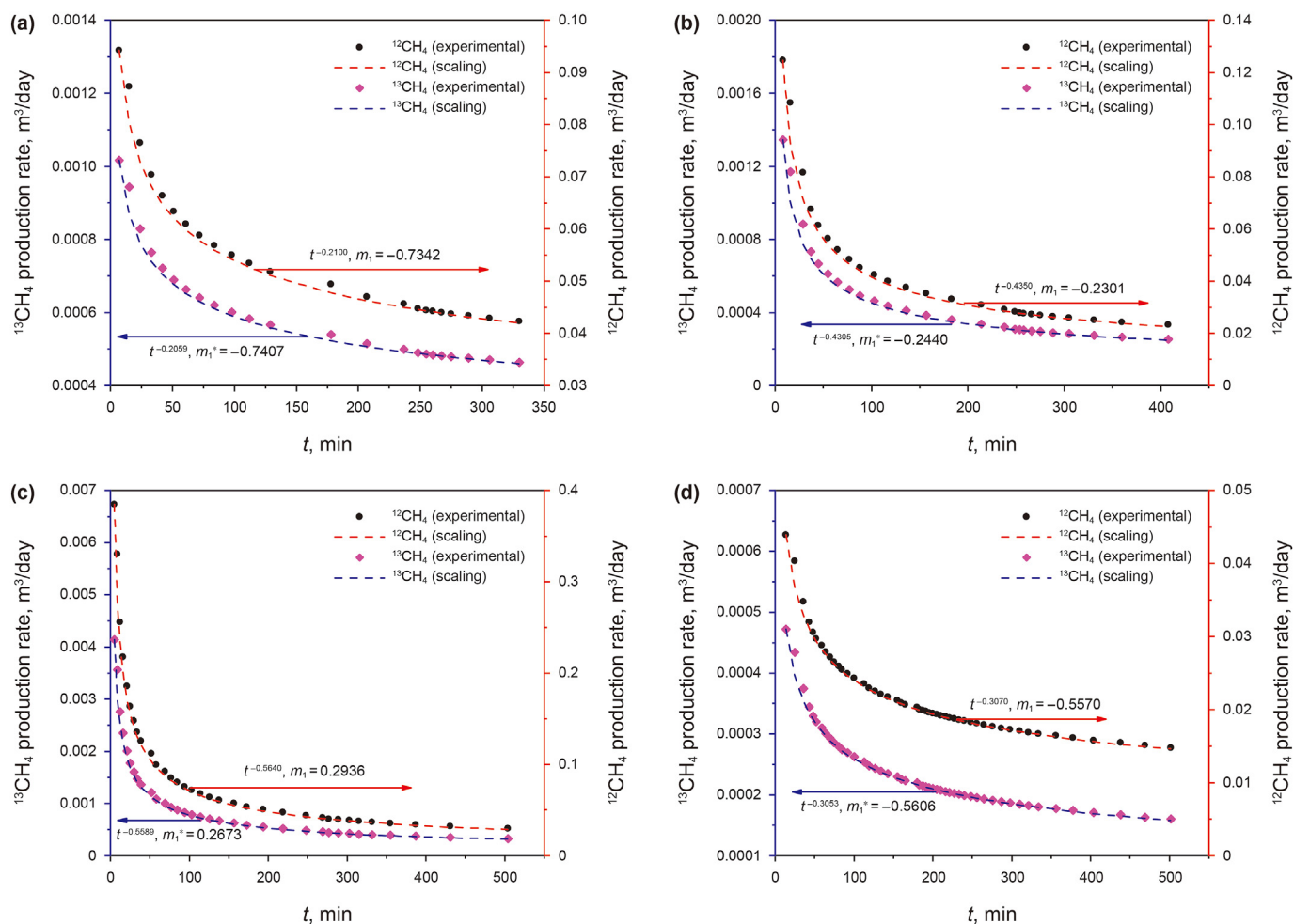

Fig. 7. Scaling methane gas production rates. (a) Weiye1, (b) Weiye2, (c) Weiye3, (d) Jinye.
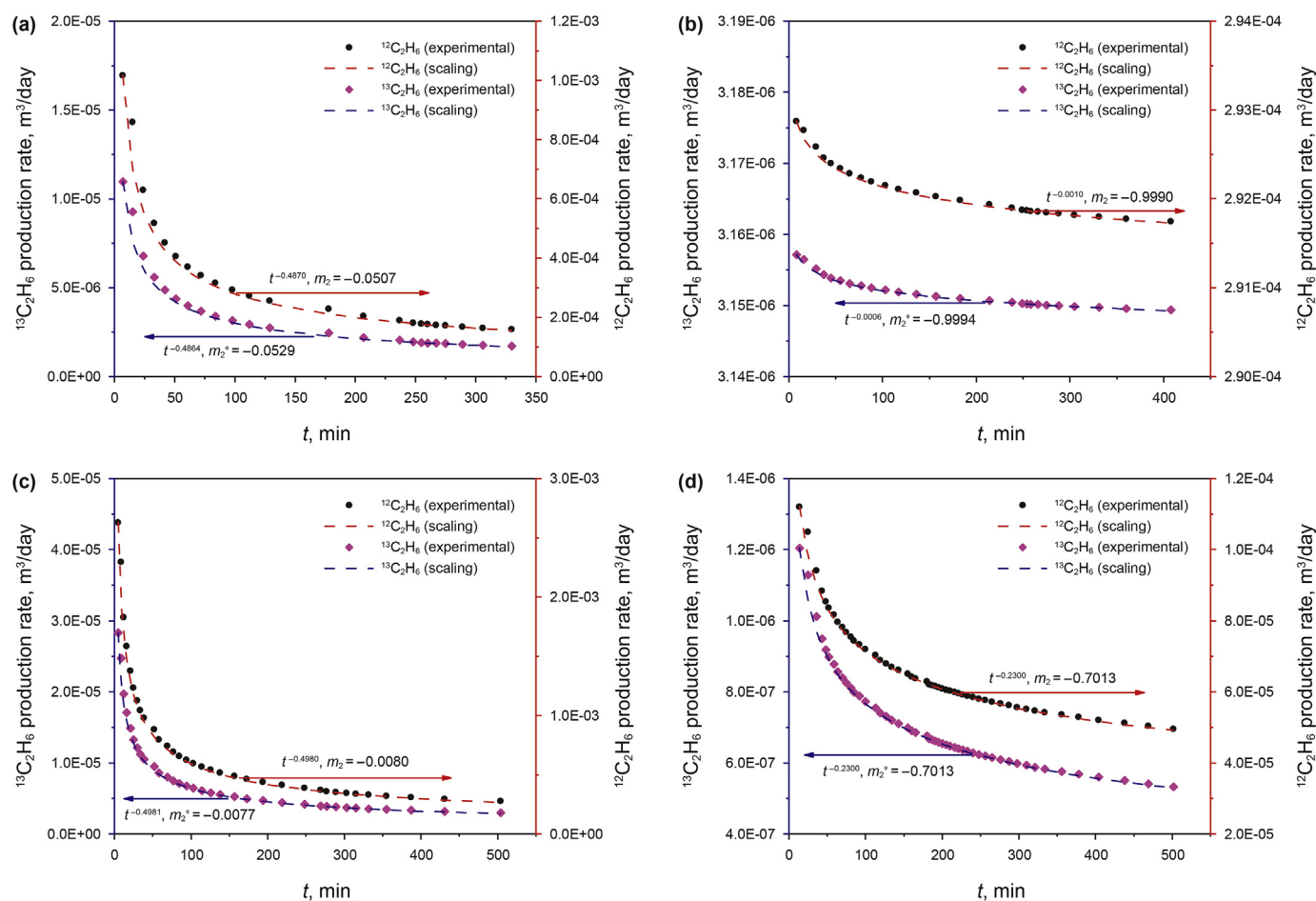
Fig. 8. Scaling ethane gas production rates. (a) Weiye1, (b) Weiye2, (c) Weiye3, (d) Jinye.

Similar to methane, the abundances of the light and heavy ethane isotopes changing with production time were obtained. Gas production rates of $^{12}C_2H_6$ of the four shale samples are $t^{-0.4870}$, $t^{-0.0010}$, $t^{-0.4980}$, and $t^{-0.307}$, with the corresponding m_2 values of -0.0529, -0.9994, -0.0077, and -0.7013. Weiye3 also shows the highest production rate of isotopic ethane gas and initial production rate (Fig. 8c), while Jinye has the lowest values (Fig. 8d). The change of the ratio of gas production rate of $^{13}C_2H_6/^{12}C_2H_6$ during the gas degassing process is very small for Weiye3 and Jinye samples (from 0.010786 to 0.010783 for Weiye3 and 0.0107531 to 0.0107529 for Jinye). This fractionation change of ethane is very small (i.e., the change of $^{13}C_2H_6/^{12}C_2H_6$ is relatively insignificant). Ethane fractionation changes are insignificant since physical mass between them is relatively low and the fractionation of ethane isotopic gases is relatively less sensitive to high Knudsen effect.

4.4.4. Magnitude of carbon isotopic reversal

Both isotopic and molecular fractionations in nano-pores occur during production (Gao et al., 2017; Zhang et al., 2018; Shi et al., 2019; Li et al., 2020). Since the magnitude of carbon isotopic reversal ($\delta^{13}C_1 - \delta^{13}C_2$) shows a positive correlation with total gas content as well as ΔK_n of methane, the scaling magnitude of carbon isotopic reversal of four samples are also developed and compared to the experimental data. It could be found that the scaling isotopic reversal matches well with the experimental fractionation data for the four shale samples (Fig. 10). The magnitude of isotopic reversal during gas degassing process has the following order: Weiye3 >

Weiye1 > Weiye2 > Jinye, which is also similar to the correlation of the total gas content. In addition, the reversal magnitude increases with production time. As discussed before, the isotopic gas fractionation inside the shale pore system is not an equilibrium process but rather a kinetic process: the lighter isotope proceeds faster through diffuse or desorption. Both the adsorption/desorption action and diffusion action combine together to affect molecular and isotopic gas fractionation. Shale with more gas content experiences a wide range of pressure drop, and gas corresponding experiences extensive degree of high K_n number diffusion. Thus, the magnitude of isotopic gas reversal (e.g., $\delta^{13}C_1 - \delta^{13}C_2$) is closely linked to the high K_n number diffusion, especially the methane isotopic gas diffusion. The exponent m, which reflects gas nonlinear diffusion properties, well indicates isotopic gas nonlinear fractionation. As a result, the mathematical model well reveals shales with high isotopic carbon reversal.

4.5. Application of the nonlinear gas flow model

The well match between the experimental and scaling results, including carbon isotope values, production rates and cumulative production of methane and ethane, shows the rationality of this self-similarity isotopic gas flow model. Thus, self-similarity mathematical model may be used to predict on-site methane and ethane isotopic gases fractionation process. By selecting appropriate exponents m and m^*, the magnitude of carbon isotopic reversal ($\delta^{13}C_1 - \delta^{13}C_2$) could be estimated. Moreover, the predicted

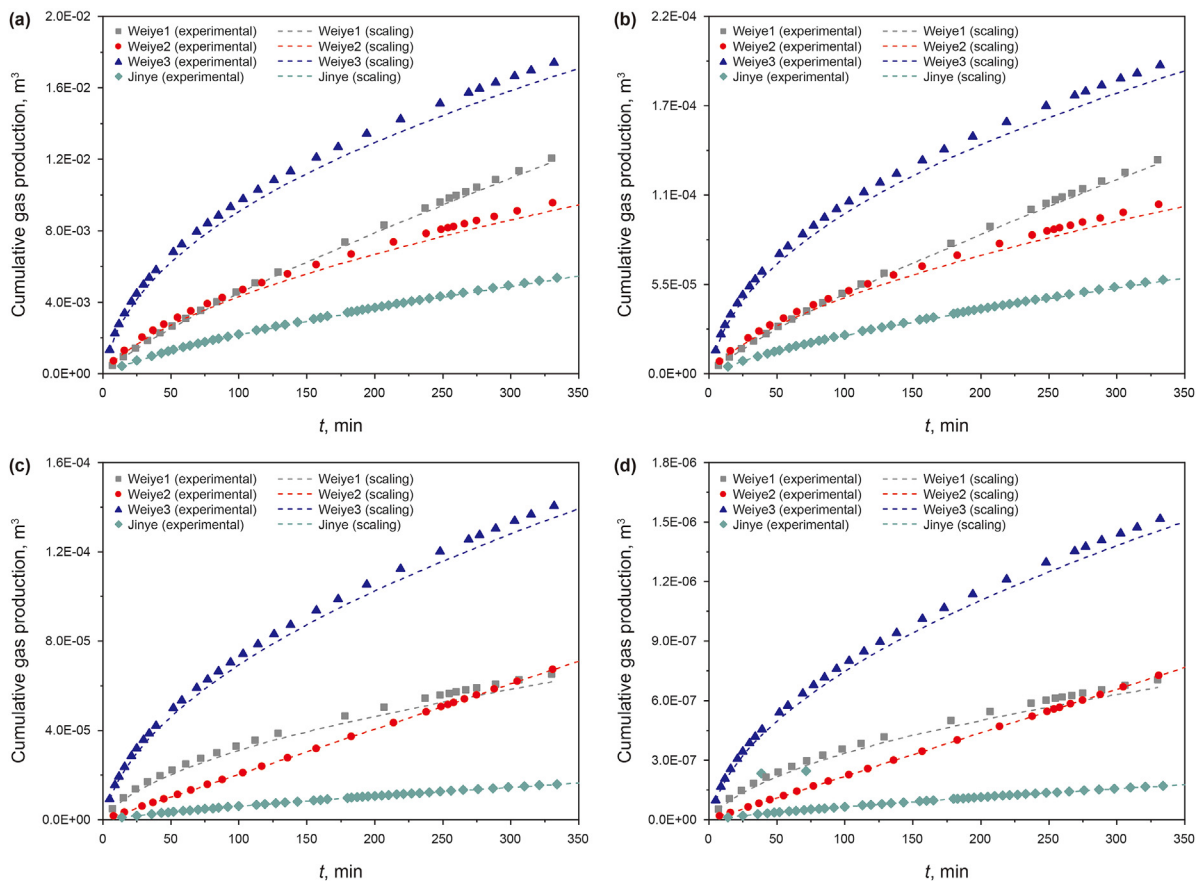**Fig. 9.** The experimental and scaling cumulative gas production of (a) $^{12}CH_4$, (b) $^{13}CH_4$, (c) $^{12}C_2H_6$ and (d) $^{13}C_2H_6$.
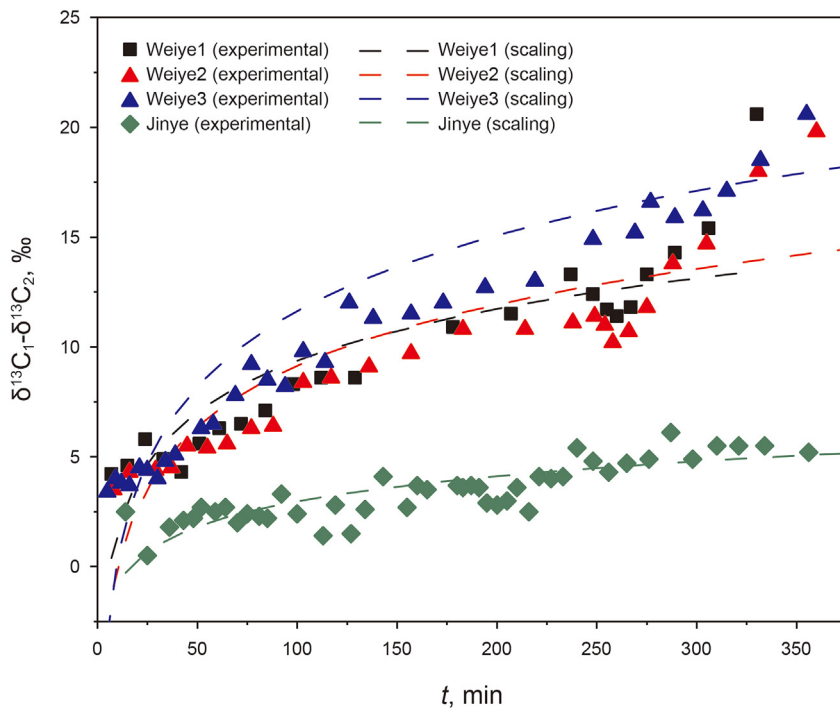

Fig. 10. Comparison of scaling carbon isotopic reversals.

$\delta^{13}C_1 - \delta^{13}C_2$ value was found to exhibit a positive relationship with total gas content. Based on these, the gas production rate decline trend could be quickly predicted and the gas storage conditions in the formation could be evaluated. Thus, this provides a simple and robust estimation method for gas exploration.

5. Conclusions

A mathematical model considering gas adsorption/desorption and diffusion was developed to simulate the methane and ethane isotopic gas fractionation. The results from the model were compared with the experimental data. Following conclusions are reached:

1. Carbon isotopic reversals ($\delta^{13}C_1 > \delta^{13}C_2$) were found for four Longmaxi shale samples. The fractionation of ethane isotopic gas ($\delta^{13}C_2$) fluctuates around $-40‰$ for all the four shale samples. However, large fractionation level of methane ($\delta^{13}C_1$) is found for the four shale samples, especially for Weiye3, which has the highest organic matter and porosity. In addition, a positive correlation is found for the total gas content and molecular fractionation deviation ($\delta^{13}C_1 - \delta^{13}C_2$).

2. The scaling carbon isotopic gas fractionation including $\delta^{13}C_1$ and $\delta^{13}C_2$ matches well with the experimental data by selecting approximate exponents (m_1, m_1^*, m_2 and m_2^*) in the mathematical model. Moreover, the scaling magnitude of isotopic reversal ($\delta^{13}C_1 - \delta^{13}C_2$) of the four samples also agrees well with the experimental one. The scaling magnitude of isotopic reversal has a positive correlation with total gas contents.

3. The difference between exponents of isotopic gas ($m_1 - m_1^*$) and ($m_2 - m_2^*$) are relatively small, indicating isotopic fractionation is a slow physical process. Besides, the value of ($m_1 - m_1^*$) are much greater than ($m_2 - m_2^*$), which means the methane molecules have a high level of fractionation variation than ethane gas.

4. Shale with high gas content experiences a wide range of high K_n diffusion flow (ΔK_n), which results in an extensive methane isotopic gas fractionation during degassing process. Weiye3 with highest gas content has the highest $\Delta m_1 - \Delta m_2$ values, and correspondingly has the highest magnitude of carbon isotopic reversals ($\delta^{13}C_1 - \delta^{13}C_2$).

Acknowledgements

Appendix

Sample properties

On-site gas composition was measured for four shale samples. Three of them were collected from Weiye shale formation, and one from Jinye formation. The samples were buried at depths between 3710 m and 3721 m. They all have high maturity with R_o greater than 2.5%. Among these four samples, Weiye3 has the highest total organic content and porosity, as well as maturity.

Table 1
Sample properties

Sample	Weiye1	Weiye2	Weiye3	Jinye
Burial depth, m	3710.02	3711.13	3720.66	3719.14
TOC, %	2.93	2.06	6.52	1.8
Maturity R_o, %	2.78	2.78	2.91	3.06
Porosity, %	5.87	5.41	6.51	2.52
Gas content, m³/t	3.07	2.76	5.35	1.76
Core length, m	0.2	0.2	0.2	0.2
Core diameter, m	0.1	0.1	0.1	0.1
Pressure coefficient	1.54	1.54	1.54	0.83
Coring time, h	10.2	12.8	9.6	10.6

References

Anderson, J.L., 1989. Colloid transport by interfacial forces. Annu. Rev. Fluid Mech. 21 (1), 61–99. https://doi.org/10.1146/annurev.fl.21.010189.000425.

Anzini, P., Colombo, G.M., Filiberti, Z., et al., 2019. Thermal forces from a microscopic perspective. Phys. Rev. Lett. 123 (2), 028002. https://doi.org/10.1103/PhysRevLett.123.028002.

Burruss, R.C., Laughrey, C.D., 2010. Carbon and hydrogen isotopic reversals in deep basin gas: evidence for limits to the stability of hydrocarbons. Org. Geochem. 41 (12), 1285–1296. https://doi.org/10.1016/j.orggeochem.2010.09.008.

Cao, C., Zhang, M., Tang, Q., et al., 2018. Noble gas isotopic variations and geological implication of Longmaxi shale gas in Sichuan Basin, China. Mar. Petrol. Geol. 89, 38–46. https://doi.org/10.1016/j.marpetgeo.2017.01.022.

Cao, G., Zhang, H., Jiang, W., et al., 2019. A new gas-content-evaluation method for organic-rich shale using the fractionation of carbon isotopes of methane. SPE J. 24 (6), 2574–2589. https://doi.org/10.2118/197043-PA.

Chen, W., Yang, Y., Wang, T., 2019. Non-linear gas transport inside an ultra-tight Longmaxi shale core under thermal stimulation conditions. Energy. 186, 115846. https://doi.org/10.1016/j.energy.2019.07.176.

Cui, X., Bustin, A.M.M., Bustin, R.M., 2009. Measurements of gas permeability and diffusivity of tight reservoir rocks: different approaches and their applications. Geofluids. 9 (3), 208–223. https://doi.org/10.1111/j.1468-8123.2009.00244.x.

Cunningham, R.E., Williams, R.J.J., 1980. Diffusion in Gases and Porous Media. Springer, Boston.

Dai, J., Zou, C., Liao, S., et al., 2014. Geochemistry of the extremely high thermal maturity Longmaxi shale gas, southern Sichuan Basin. Org. Geochem. 74, 3–12. https://doi.org/10.1016/j.orggeochem.2014.01.018.

Darabi, H., Ettehad, A., Javadpour, F., et al., 2012. Gas flow in ultra-tight shale strata. J. Fluid Mech. 710, 641–658. https://doi.org/10.1017/jfm.2012.424.

Deng, H., Hu, X., Li, H.A., et al., 2016. Improved pore-structure characterization in shale formations with FESEM technique. J. Nat. Gas Sci. Eng. 35, 309–319. https://doi.org/10.1016/j.jngse.2016.08.063.

Deng, J., Zhu, W., Qi, Q., et al., 2015. Study on the steady and transient pressure characteristics of shale gas reservoirs. J. Nat. Gas Sci. Eng. 24, 210–216. https://doi.org/10.1016/j.jngse.2015.03.016.

Di Felice, R., 2016. Knudsen diffusion. In: Drioli, E., Giorno, L. (Eds.), Encyclopedia of Membranes. Springer Berlin Heidelberg, Berlin, Heidelberg, pp. 1080–1081. https://doi.org/10.1007/978-3-662-44324-8_1293.

Ding, X., Mack Kennedy, B., Molins, S., et al., 2017. Experimental studies and model analysis of noble gas fractionation in low-permeability porous media. Geochem. Cosmochim. Acta. 205, 149–167. https://doi.org/10.1016/j.gca.2017.02.005.

El-Zehairy, A.A., Nezhad, M.M., Joekar-Niasar, V., et al., 2019. Pore-network modelling of non-Darcy flow through heterogeneous porous media. Adv. Water Resour. 131, 103378. https://doi.org/10.1016/j.advwatres.2019.103378.

Etminan, S.R., Javadpour, F., Maini, B.B., et al., 2014. Measurement of gas storage processes in shale and of the molecular diffusion coefficient in kerogen. Int. J. Coal Geol. 123, 10–19. https://doi.org/10.1016/j.coal.2013.10.007.

Feng, Z., Hao, F., Dong, D., et al., 2020. Geochemical anomalies in the lower Silurian shale gas from the Sichuan Basin, China: insights from a Rayleigh-type fractionation model. Org. Geochem. 142, 103981. https://doi.org/10.1016/j.orggeochem.2020.103981.

Ganti, R., Liu, Y., Frenkel, D., 2017. Molecular simulation of thermo-osmotic slip. Phys. Rev. Lett. 119 (3), 038002. https://doi.org/10.1103/PhysRevLett.119.038002.

Gao, J., Yu, Q., Lu, X., 2016. Apparent permeability and gas flow behavior in carboniferous shale from the Qaidam Basin, China: an experimental study. Transport Porous Media. 116 (2), 585–611. https://doi.org/10.1007/s11242-016-0791-y.

Gao, L., Wu, S., Deev, A., et al., 2017. The gas isotope interpretation tool: a novel method to better predict production decline. AAPG Bull. 101 (8), 1263–1275. https://doi.org/10.1306/09221615106.

Gao, Z., Yang, X., Hu, C., et al., 2019. Characterizing the pore structure of low permeability Eocene Liushagang formation reservoir rocks from Beibuwan Basin in northern south China Sea. Mar. Petrol. Geol. 99, 107–121. https://doi.org/10.1016/j.marpetgeo.2018.10.005.

Györe, D., McKavney, R., Gilfillan, S.M.V., et al., 2018. Fingerprinting coal-derived gases from the UK. Chem. Geol. 480, 75—85. https://doi.org/10.1016/j.chemgeo.2017.09.016.

Krooss, B.M., Leythaeuser, D., 1997. Diffusion of methane and ethane through the reservoir cap rock: implications for the timing and duration of catagenesis: discussion 1. AAPG Bull. 81, 155—161. https://doi.org/10.1306/522B42C1-1727-11D7-8645000102C1865D.

Labed, I., Oyeneyin, B., Oluyemi, G., 2018. Gas-condensate flow modelling for shale reservoirs. J. Nat. Gas Sci. Eng. 59, 156—167. https://doi.org/10.1016/j.jngse.2018.08.015.

Lei, G., Cao, N., Liu, D., et al., 2018. A non-linear flow model for porous media based on conformable derivative approach. Energies. 11 (11), 2986. https://doi.org/10.3390/en11112986.

Li, W., Lu, S., Li, J., et al., 2021. Geochemical modeling of carbon isotope fractionation during methane transport in tight sedimentary rocks. Chem. Geol. 566, 120033. https://doi.org/10.1016/j.chemgeo.2020.120033.

Li, W., Lu, S., Li, J., et al., 2020. Carbon isotope fractionation during shale gas transport: mechanism, characterization and significance. Sci. China Earth Sci. 63 (5), 674—689. https://doi.org/10.1007/s11430-019-9553-5.

Liu, J., Wang, J.G., Gao, F., et al., 2016a. Impact of micro- and macro-scale consistent flows on well performance in fractured shale gas reservoirs. J. Nat. Gas Sci. Eng. 36, 1239—1252. https://doi.org/10.1016/j.jngse.2016.05.005.

Liu, J., Wang, J.G., Gao, F., et al., 2015. Flow consistency between non-Darcy flow in fracture network and nonlinear diffusion in matrix to gas production rate in fractured shale gas reservoirs. Transport Porous Media. 111 (1), 97—121. https://doi.org/10.1007/s11242-015-0583-9.

Liu, L., Yao, J., Sun, H., et al., 2019. Compositional modeling of shale condensate gas flow with multiple transport mechanisms. J. Petrol. Sci. Eng. 172, 1186—1201. https://doi.org/10.1016/j.petrol.2018.09.030.

Liu, Y., Zhang, J., Tang, X., 2016b. Predicting the proportion of free and adsorbed gas by isotopic geochemical data: a case study from lower Permian shale in the southern North China basin (SNCB). Int. J. Coal Geol. 156, 25—35. https://doi.org/10.1016/j.coal.2016.01.011.

Ma, Y., Zhong, N., Yao, L., et al., 2020. Shale gas desorption behavior and carbon isotopic variations of gases from canister desorption of two sets of gas shales in south China. Mar. Petrol. Geol. 113, 104127. https://doi.org/10.1016/j.marpetgeo.2019.104127.

Meng, Q., Wang, X., Wang, X., et al., 2016. Variation in the carbon isotopic composition of alkanes during shale gas desorption process and its geological significance. J. Nat. Gas Geosci. 1 (2), 139—146. https://doi.org/10.1016/j.jnggs.2016.05.004.

Milkov, A.V., Etiope, G., 2018. Revised genetic diagrams for natural gases based on a global dataset of >20,000 samples. Org. Geochem. 125, 109—120. https://doi.org/10.1016/j.orggeochem.2018.09.002.

Milkov, A.V., Faiz, M., Etiope, G., 2020. Geochemistry of shale gases from around the world: composition, origins, isotope reversals and rollovers, and implications for the exploration of shale plays. Org. Geochem. 143, 103997. https://doi.org/10.1016/j.orggeochem.2020.103997.

Monteiro, P.J.M., Rycroft, C.H., Barenblatt, G.I., 2012. A mathematical model of fluid and gas flow in nanoporous media. Proc. Natl. Acad. Sci. Unit. States Am. 109 (50), 20309—20313. https://doi.org/10.1073/pnas.1219009109.

Patzek, T.W., Male, F., Marder, M., 2013. Gas production in the Barnett Shale obeys a simple scaling theory. Proc. Natl. Acad. Sci. Unit. States Am. 110 (49), 19731—19736. https://doi.org/10.1073/pnas.1313380110.

Pernaton, E., Prinzhofer, A., Schneider, F., 1996. Reconsideration of methane isotope signature as a criterion for the genesis of natural gas: influence of migration on isotopic signatures. Rev. Inst. Fr. Pét. 51 (5), 635—651. https://doi.org/10.2516/ogst:1996042.

Qin, H., Fan, X., Liu, M., et al., 2017. Carbon isotope reversal of desorbed gas in Longmaxi shale of Jiaoshiba area. Sicuhan Basin. Petrol. Res. 2 (2), 169—177. https://doi.org/10.1016/j.ptlrs.2016.11.001.

Rasoul, N.M., Mahmoud, J., 2017. Study of slip flow in unconventional shale rocks using Lattice Boltzmann method: effects of boundary conditions and TMAC. Transport Porous Media. 120 (1), 115—139. https://doi.org/10.1007/s11242-017-0912-2.

Richter, F.M., Mendybaev, R.A., Christensen, J., et al., 2005. Kinetic isotopic fractionation during diffusion of ionic species in water. Geochem. Cosmochim. Acta. 70, 277—289. https://doi.org/10.1016/j.gca.2005.09.016.

Rodriguez, N.D., Philp, R.P., 2010. Geochemical characterization of gases from the mississippian Barnett shale, fort worth basin, Texas. AAPG Bull. 94 (11), 1641—1656. https://doi.org/10.1306/04061009119.

Sano, Y., Fischer, T.P., 2013. The analysis and interpretation of noble gases in modern hydrothermal systems. In: Burnard, P. (Ed.), The Noble Gases as Geochemical Tracers. Springer Berlin Heidelberg, Berlin, Heidelberg, pp. 249—317. https://doi.org/10.1007/978-3-642-28836-4_10.

Schoell, M., 1983. Genetic characterization of natural Gases1. AAPG Bull. 67 (12), 2225—2238. https://doi.org/10.1306/ad46094a-16f7-11d7-8645000102c1865d.

Shi, W., Wang, X., Zhang, C., et al., 2019. Experimental study on gas content of adsorption and desorption in Fuling shale gas field. J. Petrol. Sci. Eng. 180, 1069—1076. https://doi.org/10.1016/j.petrol.2019.06.021.

Song, H., Yu, M., Zhu, W., et al., 2015. Numerical investigation of gas flow rate in shale gas reservoirs with nanoporous media. Int. J. Heat Mass Tran. 80, 626—635. https://doi.org/10.1016/j.ijheatmasstransfer.2014.09.039.

Strąpoć, D., Schimmelmann, A., Mastalerz, M., 2006. Carbon isotopic fractionation of CH4 and CO2 during canister desorption of coal. Org. Geochem. 37 (2), 152—164. https://doi.org/10.1016/j.orggeochem.2005.10.002.

Sun, F., Yao, Y., Li, G., et al., 2019. A slip-flow model for multi-component shale gas transport in organic nanopores. Arabian J. Geosci. 12 (5), 143. https://doi.org/10.1007/s12517-019-4303-6.

Tang, Y., Perry, J.K., Jenden, P.D., et al., 2000. Mathematical modeling of stable carbon isotope ratios in natural gases††We dedicate this paper to Bill Sackett on the occasion of his 70th birthday. Geochem. Cosmochim. Acta. 64 (15), 2673—2687. https://doi.org/10.1016/S0016-7037(00)00377-X.

Tang, Y., Xia, D., 2011. Predicting original gas in place and optimizing productivity by isotope geochemistry of shale gas. In: AAPG Hedberg Research Conference—Natural Gas Geochemistry: Recent Developments, Applications and Technologies.

Wang, Z., Wang, M., Chen, S., 2018. Coupling of high Knudsen number and non-ideal gas effects in microporous media. J. Fluid Mech. 840, 56—73. https://doi.org/10.1017/jfm.2018.46.

Wu, K., Chen, Z., Li, X., et al., 2016. A model for multiple transport mechanisms through nanopores of shale gas reservoirs with real gas effect—adsorption-mechanic coupling. Int. J. Heat Mass Tran. 93, 408—426. https://doi.org/10.1016/j.ijheatmasstransfer.2015.10.003.

Wu, K., Li, X., Wang, C., et al., 2015. Model for surface diffusion of adsorbed gas in nanopores of shale gas reservoirs. Ind. Eng. Chem. Res. 54 (12), 3225—3236. https://doi.org/10.1021/ie504030v.

Xia, X., Chen, J., Braun, R., et al., 2013. Isotopic reversals with respect to maturity trends due to mixing of primary and secondary products in source rocks. Chem. Geol. 339, 205—212. https://doi.org/10.1016/j.chemgeo.2012.07.025.

Xia, X., Tang, Y., 2012. Isotope fractionation of methane during natural gas flow with coupled diffusion and adsorption/desorption. Geochem. Cosmochim. Acta. 77, 489—503. https://doi.org/10.1016/j.gca.2011.10.014.

Xia, Y., Goral, J., Huang, H., et al., 2017. Many-body dissipative particle dynamics modeling of fluid flow in fine-grained nanoporous shales. Phys. Fluids. 29 (5), 056601. https://doi.org/10.1063/1.4981136.

Yang, Y., Wu, K., Zhang, T., et al., 2015. Characterization of the pore system in an over-mature marine shale reservoir: a case study of a successful shale gas well in Southern Sichuan Basin, China. Petroleum. 1 (3), 173—186. https://doi.org/10.1016/j.petlm.2015.07.011.

Zhang, M., Tang, Q., Cao, C., et al., 2018. Molecular and carbon isotopic variation in 3.5 years shale gas production from Longmaxi Formation in Sichuan Basin, China. Mar. Petrol. Geol. 89, 27—37. https://doi.org/10.1016/j.marpetgeo.2017.01.023.

Zhang, T., Krooss, B.M., 2001. Experimental investigation on the carbon isotope fractionation of methane during gas migration by diffusion through sedimentary rocks at elevated temperature and pressure. Geochem. Cosmochim. Acta. 65 (16), 2723—2742. https://doi.org/10.1016/S0016-7037(01)00601-9.

Zhang, T., Yang, R., Milliken, K.L., et al., 2014. Chemical and isotopic composition of gases released by crush methods from organic rich mudrocks. Org. Geochem. 73, 16—28. https://doi.org/10.1016/j.orggeochem.2014.05.003.

Zhang, W., Chen, W., Wang, T., et al., 2019. A self-similarity mathematical model of carbon isotopic flow fractionation during shale gas desorption. Phys. Fluids. 31 (11), 112005. https://doi.org/10.1063/1.5128581.

Zhang, W., Huang, Z., Li, X., et al., 2020a. Estimation of organic and inorganic porosity in shale by NMR method, insights from marine shales with different maturities. J. Nat. Gas Sci. Eng. 78, 103290. https://doi.org/10.1016/j.jngse.2020.103290.

Zhang, W., Shen, B., Chen, Y., et al., 2020b. Molecular dynamics simulations about isotope fractionation of methane in shale nanopores. Fuel 278, 118378. https://doi.org/10.1016/j.fuel.2020.118378.

Zumberge, J., Ferworn, K., Brown, S., 2012. Isotopic reversal ('rollover') in shale gases produced from the Mississippian Barnett and Fayetteville formations. Mar. Petrol. Geol. 31 (1), 43—52. https://doi.org/10.1016/j.marpetgeo.2011.06.009.